Validation of DualSPHysics for viscous Newtonian flow fronts

Suzanne Lapillonne, Georgios Fourtakas, Guillaume Piton, Guillaume Chambon, Vincent Richefeu

Validation of DualSPHysics for viscous Newtonian flow fronts

Lapillonne Suzanne*
Univ. Grenoble Alpes
INRAE, ETNA
Grenoble, France
suzanne.lapillonne@inrae.fr

Fourtakas Georgios
Univ. of Manchester
Department of Mechanical, Aero & Civil Engineering,
Manchester, United Kingdom

Piton Guillaume,
Chambon Guillaume
Univ. Grenoble Alpes
INRAE, ETNA
Grenoble, France

Richefeu Vincent
Univ. Grenoble Alpes
3SR
Grenoble, France

***Abstract*—Viscous, surging flow fronts are encountered in many applications in geophysics such as debris-, mud- and lava-flows. Few applications of the SPH method for low Reynolds, viscous flows have been rigorously validated against experimental data. In this paper, the validation of the DualSPHysics software against well documented experimental data of a laminar viscous flow front is studied. Modelling viscous Newtonian flow fronts requires the use of accurate boundary conditions, including no-slip at the wall. A convergence study analyzes the performance of the software using both bulk behaviour and front shape and detailed velocity fields along the flow. Overall, the use of the DualSPHysics solver is validated for such flows. Macroscopic dynamics and internal dynamics are well reproduced.**

I. Introduction

Viscous flow fronts, i.e., sudden transition from dry conditions to near uniform flow depth, are encountered in many applications in geophysics such as debris-, mud- and lava-flows. The precise understanding and modelling of the behaviour of such flow fronts is of interest for instance in the study of impact forces and the design of hazard mitigation measures. These highly non-uniform free-surface flows are difficult to model at front scale by classical mesh-based methods, notably due to their complex free-surface requiring remeshing which results in high computational cost. Initiatives to numerically model mud-flow fronts have been either based on depth-averaged schemes [7] which perform satisfyingly in replicating the bulk behaviour of the flow (e.g. area covered by flow spreading), but do not provide information on the internal dynamics, or, using Lagrangian methods [8], [9] which are a viable alternative on modelling flow fronts dynamics. Initial works using SPH for very viscous fluids, that are eventually non-Newtonian, are promising but lack a detailed validation against experimental campaigns. Indeed, validating SPH models against high quality experimental data for mud-like behaviour opens up the road to applications for better capturing the internal dynamics of these complex flows that are very difficult to measure experimentally and cannot be studied internally at prototype scale due to their destructive nature. Ultimately, it will allow to tailor more efficient and resistant hazard mitigation measures. An SPH solver such as DualSPHysics [2] has many advantages for geophysical applications due to explicit free-surface capturing, coupling with granular and discrete models, as well as being a highly optimised solver using GPU parallelisation techniques.

This work studies the predictions of DualSPHysics for such types of mud-flows. Validation is done against accurate measurements of the internal dynamics of flow front using data from Freydier et al. [6]. Newtonian flows are studied using the classical DualSPHysics code and the modified dynamic boundary condition (mDBC) to ensure no-slip condition.

II. SPH Modelling method

A. Governing Equations

Herein we use the continuity and Navier-Stokes equation for a weakly-compressible fluid which, in their Lagrangian form, can be written as:

$$\begin{cases} \dfrac{D\rho}{Dt} = -\rho\nabla\cdot\underline{u} & \text{(1a)} \\ \dfrac{D\underline{u}}{Dt} = \dfrac{1}{\rho}\nabla P + \dfrac{1}{\rho}\nabla\cdot\underline{\underline{\tau}} + \underline{g} & \text{(1b)} \end{cases}$$

where ρ is the density, $\underline{u}$ is the velocity, P is the pressure, $\underline{\underline{\tau}}$ is the viscous stress tensor, $\underline{g}$ represents body forces, and $\frac{D}{Dt}$ stands for the material derivative. To close this system of equation, an equation of state is used to compute the pressure P:

$$P = \frac{c_0^2\rho_0}{\gamma}\left(\left(\frac{\rho}{\rho_0}\right)^{\gamma} - 1\right) \quad (2)$$

where c_0 is the numerical speed of sound, $\gamma = 7$ and ρ_0 is the reference density. In the SPH scheme, the discrete governing equations read:

$$\begin{cases} \dfrac{\partial\rho_a}{\partial t} = \rho_a\displaystyle\sum_b(\underline{u}_a - \underline{u}_b)\cdot\nabla W_{ab}V_b + hc_0\mathcal{D}_a & \text{(3a)} \\ \dfrac{\partial\underline{u}_a}{\partial t} = -\displaystyle\sum_b m_b\left(\frac{P_a+P_b}{\rho_b\rho_a}\right)\nabla_a W_{ab} + \\ \qquad\displaystyle\sum_b m_b\left(\frac{4\nu_0\underline{r}_{ab}\cdot\nabla_a W_{ab}}{(\rho_a+\rho_b)(||\underline{r}_{ab}||^2+\eta^2)}\right)\underline{u}_a + \underline{g} & \text{(3b)} \\ \dfrac{\partial\underline{r}_a}{\partial t} = \underline{u}_a & \text{(3c)} \end{cases}$$

where subscripts a and b refer to the interpolating and neighbouring particles respectively , $\underline{r}_i$ is the positional vector of

particle i and $\underline{r}_{ij} = \underline{r}_j - \underline{r}_i$, V_i the volume occupied by the particle, m_i is the mass assigned to the numerical particle, W_{ij} is the smoothing kernel, $\eta = 0.01h$ with h the smoothing length, $\mathcal{D}_i$ is a density diffusion term (see Section II-E) and ν_0 the dynamic viscosity of the fluid.

The smoothing kernel used is the quintic Wendland kernel [12]:

$$W(r,h) = \alpha_D \left(1 - \frac{1}{2}\frac{r}{h}\right)^4 \left(2\frac{r}{h} + 1\right) \text{ for } 0 < \frac{r}{h} < 2 \quad (4)$$

where α_D depends on the dimension of the model: $\alpha_{2D} = \frac{7}{4}\pi h^2$ and $\alpha_{3D} = \frac{21}{16}\pi h^3$

B. Time-stepping

The time scheme used is the symplectic position Verlet scheme which reads [2]:

$$\begin{cases} \underline{r}_a^{n+1/2} = \underline{r}_a^n + \dfrac{\Delta t}{2}\underline{v}_a^n & (5a) \\ \underline{v}_a^{n+1/2} = \underline{v}_a^n + \Delta t \dfrac{d\underline{v}_a}{dt}^n_a & (5b) \\ \underline{v}_a^{n+1} = \underline{v}_a^n + \Delta t \dfrac{d\underline{v}_a}{dt}^{n+1/2} & (5c) \\ \underline{r}_a^{n+1} = \underline{r}_a^{n+1/2} + \Delta t \dfrac{\underline{v}_a^{n+1} + \underline{v}_a^n}{2} & (5d) \end{cases}$$

and the density evolution follows:

$$\begin{cases} \rho_a^{n+1/2} = \rho_a^n + \dfrac{\Delta t}{2}\dfrac{d\rho_a}{dt}^n & (6a) \\ \rho_a^{n+1} = \rho_a^n \dfrac{2 - \epsilon_a^{n+1/2}}{2 + \epsilon_a^{n+1/2}} & (6b) \end{cases}$$

with $\epsilon_a^{n+1/2} = -\left(\frac{d\rho_a}{dt}^{n+1/2} / \rho_a^{n+1/2}\right)\Delta t$

The actual time-step is variable to allow for optimal description of the fluid while ensuring sensible computational time. The time-step is thus taken as follows:

$$\begin{cases} dt = C_{\text{CFL}} \min(dt_1,\ dt_2,\ dt_3) & (7a) \\ dt_1 = \min_a \sqrt{\dfrac{h}{||\frac{d\underline{v}}{dt}||_{a,\max}}} & (7b) \\ dt_2 = \dfrac{h}{c_s + \max_b\left|\frac{h\underline{v}_{ab}\cdot\underline{r}_{ab}}{\underline{r}_{ab}^2 + \eta^2}\right|} & (7c) \\ dt_3 = \dfrac{h^2}{\nu_0} & (7d) \end{cases}$$

in which, dt_1 accounts for the CFL condition, dt_2 accounts for both CFL condition and the numerical viscosity and dt_3 accounts for the physical viscosity.

C. Wall Boundary condition

Due to the nature of the flow studied in this work, a no-slip condition must be imposed at the boundaries. To ensure it, *modified Dynamic Boundary Condition* (mDBC) [3] is used. No-slip condition is implemented as a correction on the velocity of fluid particles close to the boundary.

D. Shifting

Due to the nature of SPH, particles in the flow cannot maintain a relatively homogeneous distribution. Voids tend to form leading to high risks of numerical instability. In order to counteract these effects inherent to the SPH method, a shifting algorithm is used. This is particularly important for highly viscous dominated flows.

At each time step, the particles are shifted in order to maintain a more uniform particle distribution. The distance by which the particles are shifted is dependent on the concentration of particles C_i inside the kernel influence for each particle i, as well as, the velocity of the particle, as follows [10], [11]:

$$\delta r_a = -Ah||u||_a dt \nabla C_a \quad (8)$$

where A is a shifting coefficient tuned by user (the value $A = -2$ is recommended in Dominguez et al. [2]).

E. Density diffusion term

In Eq. (3a), the term $hc_0\mathcal{D}_a$ corresponds to the density diffusion term. This reduces density fluctuations, and thus oscillations in the pressure field. Indeed Eq. (2) is very stiff and with the natural disordering of SPH particles, small amplitude – high frequency oscillations are created in the pressure and density fields. In this work the density diffusion term introduced by Fourtakas et al. [4] is used:

$$\begin{cases} \mathcal{D}_a = \delta_\phi \sum_b \psi_{ab} \cdot \nabla_a W_{ab} \dfrac{m_b}{\rho_b} & (9a) \\ \psi_{ab} = 2(\rho_{ab}^T - \rho_{ab}^H) \dfrac{\underline{x}_{ab}}{||\underline{x}_{ab}||^2} & (9b) \end{cases}$$

with ρ_{ab}^T the total density, $\rho_{ab}^H = \rho_0\left(\sqrt[\gamma]{\frac{P_{ab}^H + 1}{c_0^2\rho_0/\gamma}} - 1\right)$ the hydrostatic component of the density and δ_ϕ a diffusion coefficient controlling the magnitude of this diffusion term.

III. Experimental context

A. Physical properties of the flow

The flows studied in this work are highly viscous, laminar flow fronts. Their highly non-uniform free-surface make their study very difficult using classical FEM methods, and thus SPH is a natural candidate to perform accurately for such flows.

The focus of this work is on a viscous laminar flow front with Reynolds number close to the creeping flow limits ($Re \approx 0.1$). These flow front are assumed to be composed of a non-uniform front followed by a uniform zone, where the free surface elevation $z_{\max}$ becomes steady longitudinally $\partial_x z_{\max} = 0$.

At the lowest order, the flow pressure can be assumed as :

$$p = \rho g \cos\theta (z_{\max} - z) \quad (10)$$

which gives the following force balance :

$$\rho g \sin\theta - \partial_x p + \partial_z \tau_{xz} = 0 \quad (11)$$

TABLE I: Characteristics of the experiment, density ρ [kg $\cdot$ m^{-3}], viscosity μ [Pa $\cdot$ s], slope angle θ [°], conveyor belt velocity u_b [mm $\cdot$ s^{-1}], Reynolds number Re [–]

exp. ID	ρ	μ	θ	u_b	Re
150506	1383	5.6	15.3	75	0.34

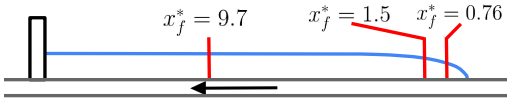

Fig. 1: Flow front modelled in DualSPHysics, three different positions are studied precisely to be compared to the experimental data

which, integrated along z gives:

$$\tau_{xz} = \mu \frac{\partial u_x}{\partial z} = \rho g \sin\theta (1 - \cot\theta \partial_x z_{\max})(z_{\max} - z) \quad (12)$$

giving the following velocity profile and average velocity in the uniform zone, with $\alpha = \frac{\rho g \sin\theta}{\mu}(1 - \cot\theta \partial_x z_{\max})$:

$$\begin{cases} u_x(z) = \alpha(z_{\max} - \frac{1}{2}z)z & (13a) \\ \bar{u_x} = \frac{\alpha}{3} z^2_{\max,\ \text{unif}} & (13b) \end{cases}$$

B. Selected experimental setup

The setup chosen for this validation is the experimental work by Freydier [5]. The characteristics of the experiments used as referenced are shown in Table I. The experimental setup is composed a conveyor belt tilted to a chosen angle, transparent side-walls, and a wall upstream the conveyor belt forcing a flow front to form steadily. This setup is thoroughly described in [1], [6]. Fluids used are transparent mixtures of glucose and water allowing to measure accurate velocity fields and free surface profiles. Freydier [5] showed that these flows have a viscosity independent from strain and strain-rate, varying with concentration of glucose in the mixture. They are also highly influenced by drying [5], leading to uncertainties on the measured viscosity in a rheometer.

Velocimetry using STV technique (see Freydier [5]), and high definition, high velocity cameras at different location of the flow allows for a full description of both the free surface shape and the velocity fields within the flow.

C. Numerical setup

The numerical setup reproduces the experimental setup as a 2D flow front (Fig. 1). The 2D assumption is possible thanks to the tests operated by Freydier [5]. Volume of the experiment has been respected and the flow height is initialized at the theoretical height of the uniform zone (from Eq. 13*b*).

The conveyor belt starts a backwards motion in a periodic domain after a short resting time, using a ramp to reach the velocity of the experiment in order to avoid any instabilities caused by the sudden infinite acceleration of an instantaneous motion.

TABLE II: Numerical parameters of the convergence study

d_p (m)	0.001	0.0005	0.00025		
C_h $(-)$	1	1.3	1.5	1.8	2.2

The initial particle spacing allows for the flow front to have at least 15 particles in depth.

A full convergence study is made, including convergence in both d_p the particle spacing distance and C_h the smoothing coefficient applied in the simulation according to Table II.

The validation of the behaviour of the flow will be regarded as the accuracy to represent : the bulk flow behaviour as per (*i*) the velocity of the flow front, (*ii*) the free-surface elevation in the uniform zone and (*iii*) the free-surface shape, but also the internal kinetic of the flow through (*iv*) the velocity profiles at 3 different locations in the flow front (Fig. 1) and as provided by Freydier et al. [6].

IV. Results

A. Data processing

The numerical model is run for a sufficient period of time, ensuring steady state to be reached. For each error calculation, the results are averaged over a few seconds to obtain more representative data.

For all results, heights and lengths are normalized by h_n, the theoretical flow height in the uniform zone so that $h^* = h/h_n$ and $x^* = x/h_n$. This theoretical flow height is derived from Eq. 13b and is taken as $h_n = 18.6$ mm. The velocities are normalized by the average velocities, *i.e.*, by the velocity of the conveyor belt u_b so that $u^* = u/u_b$. It is important to note that due to the numerical setup, the flow front is immobile in the eye of the observer. For more clarity, the reference frame is put back in the Eulerian framework so that $u_{\text{numerical}} = u_{\text{sim}} + u_b$ where u_{sim} is the raw results from the simulation.

B. Macro-dynamics of the flow

The primary interest of the validation is the macro behaviour of the flow. Looking at the front velocity error gives us the performance of DualSPHysics on modelling such flows at the surge scale. The error (i) on the velocity of the flow front is characterized as:

$$\zeta_f = \frac{|u^*_{f,\text{numerical}} - u^*_b|}{u^*_b} \quad (14)$$

where $u^*_{f,\text{numerical}}$ is the normalized velocity provided by the numerical model averaged over one second, taken as the derivative of the location of the toe of the front.

This error is expected to be null as the velocity u^*_b is set to the theoretical value of the flow front velocity.

In Fig. 2, ζ_f is plotted for three different d_p values and four different C_h values. For the finest resolution, the error on the velocity of the front and thus location of this front becomes less than 1% for three smoothing coefficients which is acceptable for mud-flows behavior, considering the uncertainty on field and experimental measurements with which our future simulations will be compared. Overall, convergence

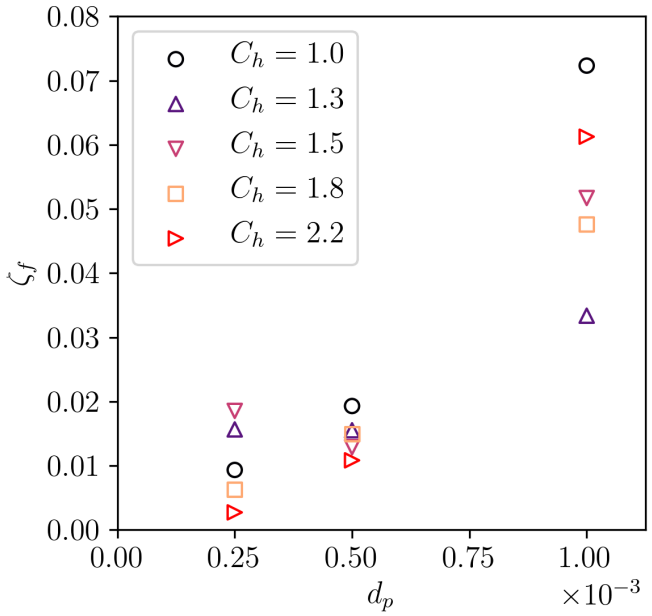

Fig. 2: Error on the flow front velocity as defined in Eq. 14, d_p in m

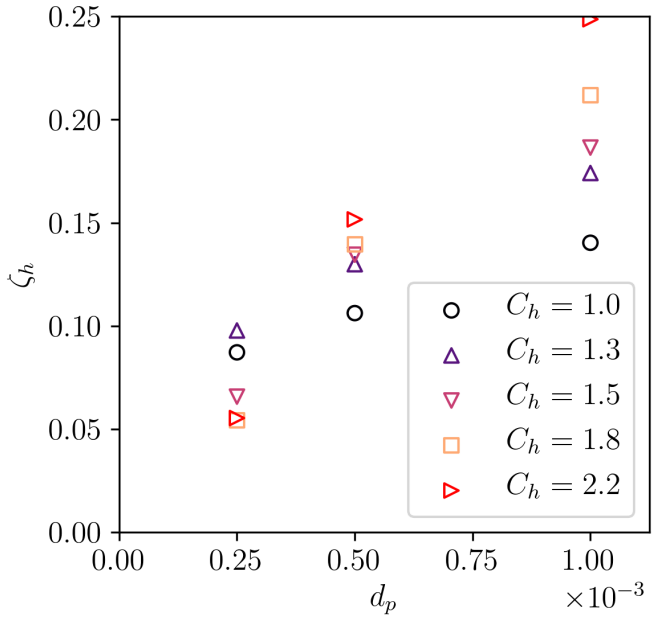

Fig. 3: Error on the free surface elevation in the uniform zone as defined in Eq. 15, d_p in m

of the model is shown on this figure and highest smoothing coefficients render better results.

In the uniform zone (upstream from the front), the height of the flow should reach the theoretical value, for which $\partial_x z = 0$. In this zone (taken as $x^* > 9$), the error (ii) on the free surface elevation is:

$$\zeta_h = \frac{|h^*_{u,\text{numerical}} - h^*_n|}{h^*_n} \tag{15}$$

where $h^*_{u,\text{numerical}}$ is the normalized height in the uniform zone.

In Fig. 3, ζ_h is plotted for numerical convergence. It is shown that the numerical solution converges and the error is diminished to only 5% of the theoretical value, which is largely acceptable for the applications this project is intended for.

Free surface profile is also of interest to be accurately reproduced for geophysical applications. Access to experimental accurate measurements of the free surface shape from the toe of the front to the uniform zone, as provided by Freydier in [5] is rare. To characterize globally the performance of DualSPHysics in reproducing the shape of the flow front, a root mean squared error on the free surface elevation (iii) is computed as follows:

$$\zeta_{fs} = \sqrt{\sum_x \frac{\left(z_{\text{max, Freydier}}(x) - z_{\text{max, num}}(x)\right)^2}{N_x}} \tag{16}$$

where N_x is the number of points on the front shape measurements provided by Freydier [5].

In Fig. 4, ζ_{fs} is plotted against different resolution schemes. Overall convergence is achieved, and errors become insignificant particularly for $(C_h,\ d_p) \in [(1.8,\ 0.25 \cdot 10^{-3}),\ (2.2,\ 0.25 \cdot 10^{-3})]$. Note the stong influence of the

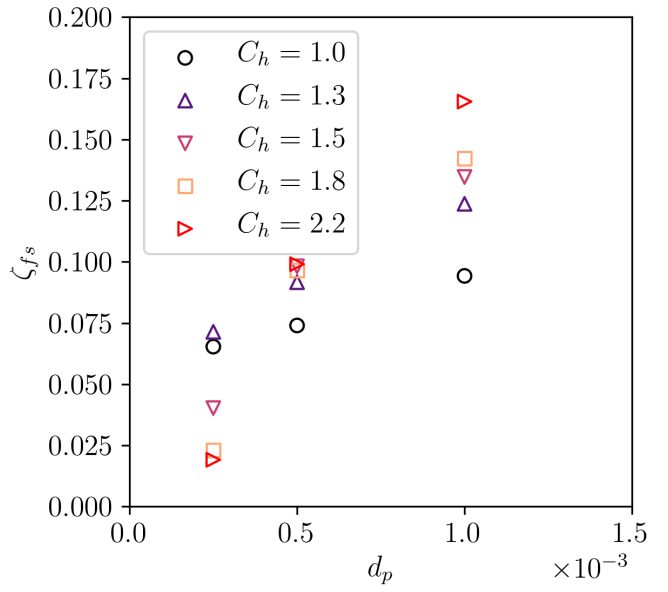

Fig. 4: Root mean squared error on the surface shape for different resolutions and smoothing coefficient as defined in Eq. 16, d_p in m

smoothing coefficient on the error value: this is a reminder that C_h drives not only the numerical computation but the free-surface detection too. In applications where the free surface is very variable, and is the focus of the study, the value of the smoothing coefficient must be thoroughly investigated.

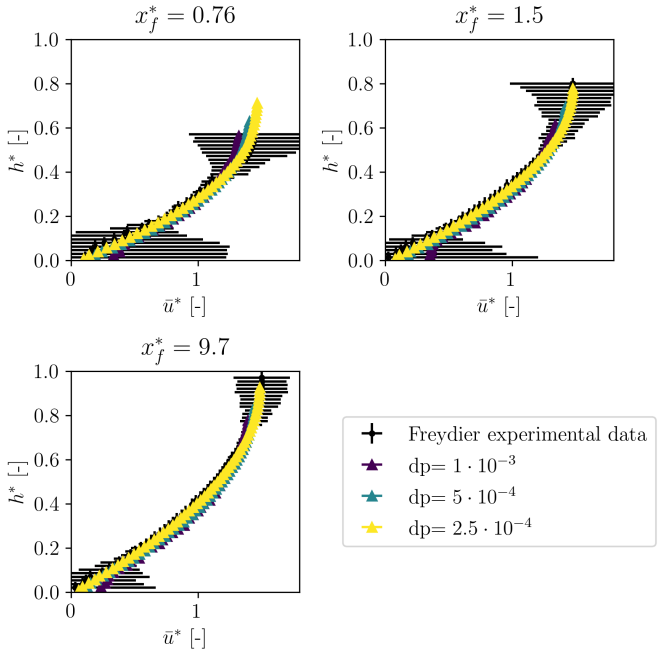

Fig. 5: Velocity profile convergence for $C_h = 1.8$ at three different locations in the front : $x_f^* = 0.76$ and $x_f^* = 1.5$ being close to the front tip, where $\partial_x z$ is significant, and $x_f^* = 9.7$ in the uniform zone, d_p in m

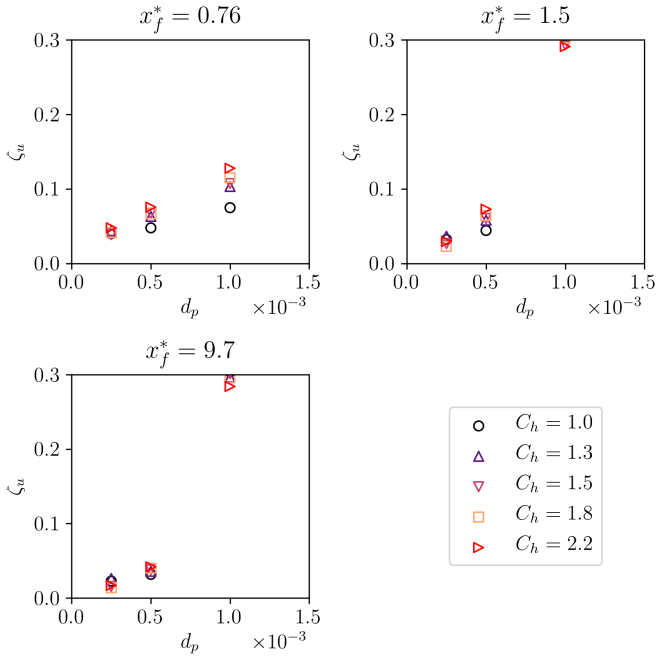

Fig. 6: Root mean squared error as defined in Eq. 17 on the velocity profiles at three different locations in the front: $x_f^* = 0.76$ and $x_f^* = 1.5$ being close to the front tip (*i.e.*, where $\partial_x z \neq 0$), and $x_f^* = 9.7$ in the uniform zone (*i.e.*, where $\partial_x z \approx 0$), d_p in m

C. Internal dynamics of the flows

Not using depth-averaged methods also enable to study precisely how accurately the model reproduce the velocity profiles which will drive the impact load for instance. The velocity profiles are studied at three different locations shown in Fig. 1. The abscissas are defined relatively to the toe of the front.

In Fig. 5, the velocity profiles for $C_h = 1.8$ are plotted for each location and resolution. The overall behaviour of the flow is well reproduced for all resolutions. Profiles are well within the error bars of the experimental data. Discrepancies on the height of the flow for $x_f^* = 0.76$ are due to the experimental measurements : close to the free-surface, access to the velocity of the flow, especially near the free surface, becomes difficult, as stated by Freydier in [5] making measurements in this section of the flow less accurate.

Even near the front, the shape of the velocity profile is accurately reproducing the dynamics, and allows to access to precise velocity mapping, which is rarely available experimentally, and not available using classical depth-averaged models.

A global criterion to characterize the convergence, for each of the location j is needed. A global root mean squared error of the velocity field (ii) is thus defined:

$$\zeta_{u,j} = \sqrt{\sum_z \frac{(u^*_{j,\text{Freydier}}(z) - u^*_{j,\text{num}}(z))^2}{N_{z,j}}} \qquad (17)$$

where $N_{z,j}$ is the number of points in the vertical direction.

In Fig. 6, $\zeta_{u,j}$ for each (d_p, C_h) is plotted. Convergence is shown for each smoothing coefficient. The convergence is similar regardless of the choice of a smoothing coefficient C_h, and overall, the error becomes smaller than 5% when using the finest resolution which is acceptable considering the precision of the experimental measurements.

V. Discussion

The accuracy of the results at different points in the flow show promising results in terms of possible applications, especially close to the toe of the front. Precise knowledge about the flow front characteristics is of major interest for applications on mud-flow behaviour as well as debris flow modeling.

A. Acceptability of the residual errors

The residual errors presented above could be further investigated using finer resolutions. Although this is of interest for theoretical convergence studies, this work is intended as an application project. The cost over benefit ratio of studying finer schemes becomes significantly less interesting in resolutions that are finer than ones presented in Table I. The knowledge on experimental data and data uncertainty for such mud-flows and debris flows in the field leads us to consider acceptable this error and consider it as an uncertainty of the numerical method in further applications.

(a) Skillen et al. [11] (b) Lind et al. [10]

Fig. 7: Comparison of the particle spatial distribution for the two shifting methods for $d_p = 0.25 \cdot 10^{-3}$ m and $C_h = 1.8$

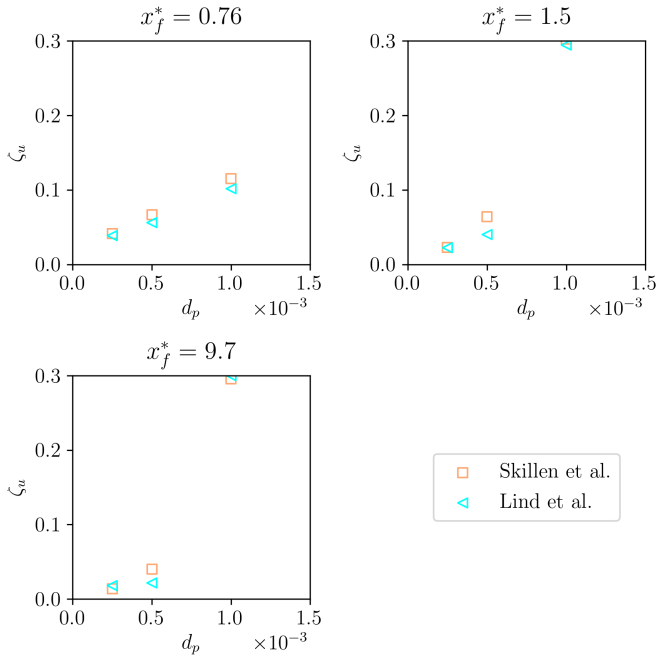

Fig. 8: Comparison of ζ_u for the shifting methods at three different positions in the front : $x_f^* = 0.76$ and $x_f^* = 1.5$ being close to the front tip, where $\partial_x h$ is significant, and $x_f^* = 9.7$ in the uniform zone, d_p in m

B. *Shifting method*

Although convergence is confirmed for the numerical model, ζ_h stays above 5% for the computed cases. Finer resolutions are investigated in the frame of convergence but on Fig 7(a), the particle spatial distribution at a given time step is shown. One can note that the particle distribution with this simulation forms layers near the front, distributing the particles along lines, eventually leading to instabilities in the pressure profile. In addition, there is a layer of particles at the bottom of the flow where a vertical ordering of the particles can be seen. This leads to the hypothesis that the formulation of shifting by Skillen at al. [11] already implemented in the release version of DualSPHysics is not the optimal formulation for this application. Indeed, the non-uniform nature of this flow, coupled with the strong no-slip condition at the bottom of the channel leads to large differences in velocity magnitude

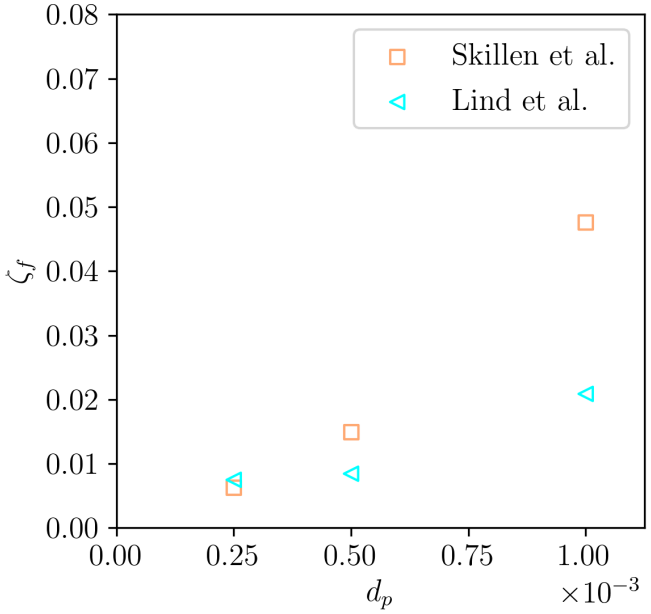

Fig. 9: Comparison of ζ_f for the shifting methods, d_p in m

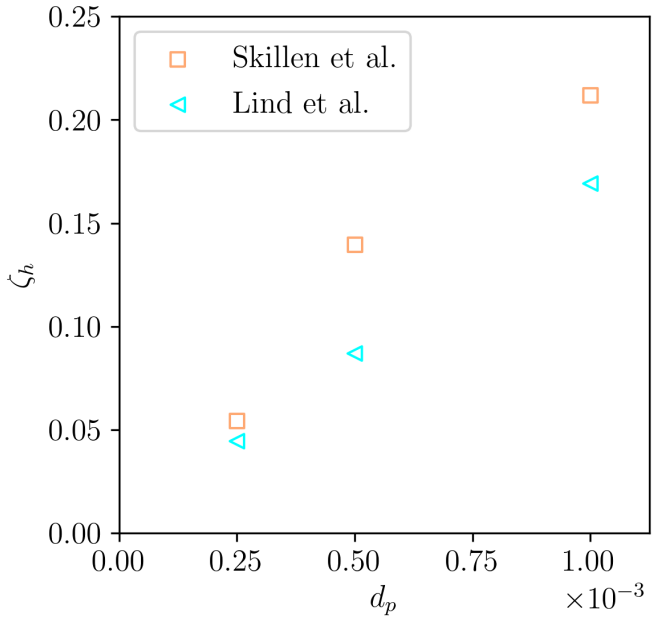

Fig. 10: Comparison of ζ_h for the shifting methods, d_p in m

within the flow, especially having zones where the velocity is almost null. A shifting method proportional to the velocity magnitude then leads to a very uneven shifting in the flow, and thus to such patterns in the velocity profile.

As an alternative, the shifting formulation by Lind et al. [10] is used:

$$\delta r_a = -\frac{A_l}{2} h^2 dt \nabla C_a \tag{18}$$

In this method, particles within $C_h \cdot h$ of the detected free

surface are not shifted. On Fig. 7(b), the particle distribution at the front for the shifting method of Lind et al [10] is shown. It is much smoother and less ordered near the free surface as expected. On Fig. 9 and 10, comparison of the different shifting methods for $C_h = 1.8$ is plotted against the flow front velocity and the uniform flow depth, respectively. The shifting method by Lind et al. [10] performs better, impacting positively the bulk behavior of the flow. On the other hand, Fig 8 shows that the shifting method marginally affects the performance of the velocity profile error ζ_u, while still ensuring satisfactory results.

In essence, this study demonstrates that this alternative method shows better results comparatively and these preliminary results show that a reflection on the shifting method is of major importance for such applications with very viscous, though surging flows, where velocities are null locally, and velocity gradient highly varies across the flow.

VI. Conclusion

In this work, we validated the results of DualSPHysics against accurate flow measurement of very viscous flows having a surging behaviour, *i.e.*, steep free surface profiles. Overall, the global behavior of the front, as well as the dynamics of the flow, are well reproduced by the DualSPHysics solver. We additionally show that another shifting method than the classical one implemented in the release version of DualSPHysics is better suited, probably due to the peculiarities of these flows, notably their locally very low velocities. Applications of the DualSPHysics solver in mud-flows opens up a lot of possibilities for prototype-scale modeling to study e.g., impact forces and interaction with structures. The advantages of the DualSPHysics software, including its highly parallelized implementation, its growing community and the many coupling currently in place make it a good candidate for more application in the field of debris flow and mud-flow investigations.

VII. Acknowledgment

This project has received funding by the Labex TEC21 (Investissements d'Avenir program, grant agreement ANR-11-LABX-0030).

References

[1] G. Chambon, A. Ghemmour, and D. Laigle. Gravity-driven surges of a viscoplastic fluid: An experimental study. *Journal of Non-Newtonian Fluid Mechanics*, 158(1):54–62, 2009. Visco-plastic fluids: From theory to application.

[2] J. M. Domínguez, G. Fourtakas, C. Altomare, R. B. Canelas, A. Tafuni, O. García-Feal, I. Martínez-Estévez, A. Mokos, R. Vacondio, A. J. C. Crespo, B. D. Rogers, P. K. Stansby, and M. Gómez-Gesteira. DualSPHysics: from fluid dynamics to multiphysics problems. *Computational Particle Mechanics*, 2021.

[3] A. English, J. Domínguez, R. Vacondio, A. Crespo, P. Stansby, S. Lind, L. Chiapponi, and M. Gómez-Gesteira. Modified dynamic boundary conditions (mdbc) for general-purpose smoothed particle hydrodynamics (sph): application to tank sloshing, dam break and fish pass problems. *Computational Particle Mechanics*, 04 2021.

[4] G. Fourtakas, J. M. Dominguez, R. Vacondio, and B. D. Rogers. Local uniform stencil (lust) boundary condition for arbitrary 3-d boundaries in parallel smoothed particle hydrodynamics (sph) models. *Computers Fluids*, 2019.

[5] P. Freydier. *Dynamique interne au front d'écoulements à surface libre. Application aux laves torrentielles*. PhD thesis, 2017.

[6] P. Freydier, G. Chambon, and M. Naaim. Experimental characterization of velocity fields within the front of viscoplastic surges down an incline. *Journal of Non-Newtonian Fluid Mechanics*, 240:56–69, 2017.

[7] D. Laigle and P. Coussot. Numerical modeling of mudflows. *Journal of Hydraulic Engineering*, 123(7):617–623, 1997.

[8] D. Laigle and M. Labbe. SPH-based numerical study of the impact of mudflows on obstacles. *International Journal of Erosion Control Engineering*, 10:12, 2017.

[9] A. Leonardi, F. K. Wittel, M. Mendoza, and H. J. Herrmann. Coupled DEM-LBM method for the free-surface simulation of heterogeneous suspensions. *Phys. Rev. E*, 1(1):3–13.

[10] S. J. Lind, R. Xu, P. K. Stansby, and B. D. Rogers. Incompressible smoothed particle hydrodynamics for free-surface flows: A generalised diffusion-based algorithm for stability and validations for impulsive flows and propagating waves. *Journal of Computational Physics*, 231(4):1499–1523, 2012.

[11] A. Skillen, S. Lind, P. K. Stansby, and B. D. Rogers. Incompressible smoothed particle hydrodynamics (sph) with reduced temporal noise and generalised fickian smoothing applied to body–water slam and efficient wave–body interaction. *Computer Methods in Applied Mechanics and Engineering*, 265:163–173, 2013.

[12] H. Wendland. Piecewise polynomial, positive definite and compactly supported radial functions of minimal degree. *Advances in computational Mathematics*, 4(1):389–396, 1995.